Geophysical Journal International

Rapid lateral variation of *P*-wave velocity at the base of the mantle near the edge of the Large-Low Shear Velocity Province beneath the western Pacific

Satoru Tanaka,[1] Hitoshi Kawakatsu,[2] Masayuki Obayashi,[1] Y. John Chen,[3] Jieyuan Ning,[3] Stephen P. Grand,[4] Fenglin Niu[5] and James Ni[6]

[1]*Department of Deep Earth Structure and Dynamics Research, Japan Agency for Marine-Earth Science and Technology, Yokosuka, Japan.*
E-mail: stan@jamstec.go.jp
[2]*Earthquake Research Institute, University of Tokyo, Tokyo, Japan*
[3]*Institute of Theoretical and Applied Geophysics, School of Earth and Space Sciences, Peking University, Beijing, China*
[4]*Department of Geological Sciences, The University of Texas at Austin, Austin, TX, USA*
[5]*Department of Earth Science, Rice University, Houston, TX, USA*
[6]*Department of Physics, New Mexico State University, Las Cruces, NM, USA*

SUMMARY
We examine *P*-wave velocity structure at the base of the mantle beneath the western Pacific, near the western edge of the Pacific Large-Low Shear Velocity Province (LLSVP), using high-quality seismograms provided by a large-scale mobile broad-band seismic observation in northeastern China (the NECESSArray project). Forward modelling using the reflectivity method is conducted to explain the variation of *P*-wave traveltimes as a function of epicentral distance near the core shadow zone. Additionally, PcP–P traveltimes are examined to enlarge the survey area. As a result, a rapid variation of *P*-wave velocity is detected at the base of the mantle. Regions of thin (20–50 km thick) and low velocity (−2 to −5 per cent) layers at the base of the mantle are intersected by an 80-km-thick region with a high velocity (+2 per cent). A slightly fast region exists at the northwest of the region with the thin low-velocity layer. These layers are typically separated by several hundred kilometres and would be difficult to explain by thermal effects alone. These observations suggest that very complicated thermochemical reactions occur near the edge of the Pacific LLSVP.

Key words: Composition of the mantle; Body waves; Pacific Ocean.

1 INTRODUCTION

Lower mantle dynamics have been extensively examined using 3-D *S*-wave velocity structures rather than *P*-wave velocity structures (McNamara & Zhong 2005; Simmons *et al.* 2006; Steinberger & Calderwood 2006; Yoshida 2008, 2012). This is partly because, besides direct *S*-waves, other phases such as ScS and SKS, which traverse the lower mantle, are widely observed and can therefore be used for tomographic inversions to result in better global coverage. *S*-waves are also used because the velocity decrease of *S*-waves in hot subducted crusts in the lower mantle is theoretically expected to be much larger than that of *P*-waves (Tsuchiya 2011) and therefore easier to detect. Based on 3-D *S*-wave velocity features, the edge of the Large-Low Shear Velocity Provinces (LLSVPs) in the lower mantle beneath Pacific and Africa is thought to be the possible source locations of mantle plumes (Burke *et al.* 2008; Garnero & McNamara 2008; Tan *et al.* 2011). However, both *P*- and *S*-wave velocity structures are important to fully understand the thermochemical dynamics of the mantle (Wysession *et al.* 1992; Montelli

et al. 2004; Boschi *et al.* 2007; Boschi *et al.* 2008; Steinberger & Holme 2008).

The LLSVPs in the lower mantle beneath Pacific and Africa had been identified even in the pioneering works of *P*-wave tomography (Dziewonski 1984; Inoue *et al.* 1990). Recent *P*-wave global tomographic results, especially focusing on the core–mantle boundary (CMB), indicate that the magnitude of the velocity reductions and pattern of these low velocity regions are not always similar, probably owing to the differences of phases used and their quality (Zhao 2004; Houser *et al.* 2008; Soldati *et al.* 2012; Young *et al.* 2013). Furthermore, the radial resolution at the base of the mantle remains poor. For instance, even in the recent global models, an approximately 300-km-thick layer is assigned at the base of the mantle.

Most recently, Frost & Rost (2014) revealed the northern and eastern edge of *P*-wave velocity structure around the Pacific LLSVP by USArray. However, understanding of the detailed *P*-wave velocity structure near the western edge of the Pacific LLSVP has been still quite limited, where detailed *S*-wave velocity structures
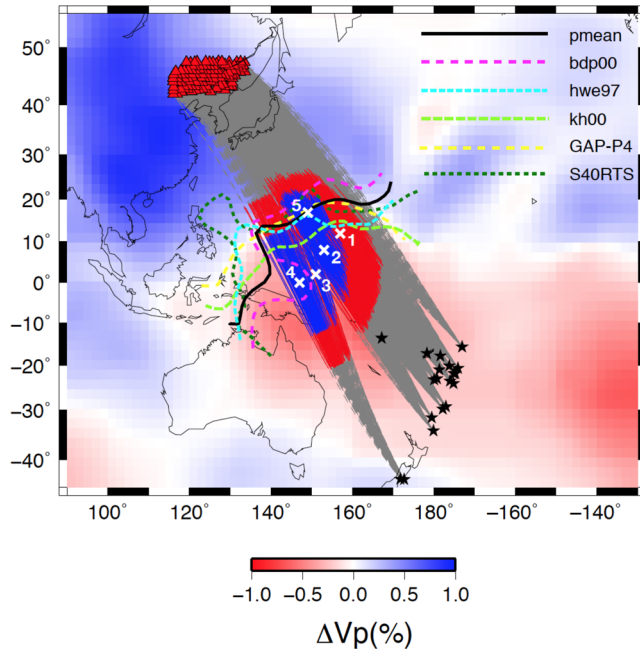
Figure 1. Geographical distribution of seismic stations (triangles), epicentres (stars), seismic rays and zero contours of *P*-wave velocity perturbations beneath the western Pacific. Red and blue background colours are *P*-wave velocity perturbations at the base of the mantle taken from the GAP-P4 model (Obayashi *et al.* 2013). White crosses with numbers indicate representative regions. Blue, red and grey lines of seismic ray paths represent the ray portion passing through the lowermost 100 km, 300 km of the mantle and the above, respectively. The yellow, purple, light blue and green broken lines and the thick black line represent the zero contours of *P*-wave velocity perturbations taken from the models of GAP-P4, bdp00 (Antolik *et al.* 2001), hwe97 (van der Hilst *et al.* 1997), kh00 (Karason & van der Hilst 2001) and pmean (Becker & Boschi 2002), respectively. The dark green short broken line is the zero counter of *S*-wave velocity perturbation taken from the model of S40RTS (Ritsema *et al.* 2011).

have been examined by many researchers (He *et al.* 2006; Takeuchi *et al.* 2008; He & Wen 2009; Idehara *et al.* 2013). Owing to limited source–receiver combinations, previous studies focussed on *P*-wave velocity structure at the base of the mantle in the middle of the LLSVP beneath the western Pacific using PdP and PcP waves. These studies used the Fiji earthquakes observed by Japanese dense seismic networks and obtain no evidence for ultralow-velocity zones (ULVZs; Shibutani *et al.* 1993; Yamada & Nakanishi 1996, 1998; Kito & Kruger 2001; Kito *et al.* 2004). Thus additional observations are required to extend the survey area. This study uses the NECES-SArray (NorthEast China Extended SeiSmic Array), a large-scale mobile broad-band seismic array comprising 120 stations in northeastern China, operating from 2009 to 2011. Such a large aperture array covers a relatively long-distance range to give constraints on radial velocity structure. *P*-waves near the core shadow zone and PcP waves from southwestern Pacific earthquakes are observed by NECESSArray, passing through the bottom of the mantle near the western edge of the Pacific LLSVP. In this study, we examine *P*-wave traveltimes near the core shadow zone, as well as PcP–P traveltimes, to determine the *P*-wave velocity structure in the lowermost 100 km or less of the mantle. This study reveals the presence of a distinct lateral variation, whose implications will be discussed further.

2 DATA

NECESSArray is a passive broad-band seismic experiment, extending approximately 1200 km from east to west and 600 km from north to south with the average spacing of approximately 80 km (Fig. 1), which is an international collaboration between China, United States and Japan. The primary objectives of the experiment are to investigate the feature and fate of the subducted Pacific slab (Obayashi *et al.* 2011; Takeuchi *et al.* 2014; Tang *et al.* 2014) and determine the structure of the Northeastern China craton (Tao *et al.* 2014; Ranasinghe *et al.* 2015). Additionally, this array is a powerful tool for studying deep Earth structures. This study utilizes the

Table 1. Event list.

Event	Date	Time (UTC)	Lat. (°)	Long. (°)	Depth (km)	m_b	Remarks
1	20091010	19:41:24.27	−15.660	−173.063	13.0	5.6	S R
2	20091025	07:53:52.15	−23.091	−179.205	417.9	5.6	S R
3	20091102	10:47:13.24	−24.121	−175.173	9.0	6.1	S R
4	20091109	10:44:55.11	−17.239	178.331	595.0	6.5	S R
5	20091112	02:13:37.58	−20.979	−178.662	570.6	5.2	S R
6	20091122	07:48:20.61	−17.794	−178.425	522.6	5.7	S R
7	20091122	22:47:27.48	−31.569	179.467	435.7	5.7	S R T
8	20091124	12:47:15.66	−20.708	−174.035	18.0	6.4	S R
9	20091128	09:21:17.98	−29.216	−177.018	28.0	5.8	S R
10	20100207	22:28:20.66	−23.319	−179.877	544.0	5.6	S R
11	20100304	14:02:27.55	−13.571	167.227	176.0	6.5	PcP
12	20100410	16:54:24.25	−20.114	−176.223	273.2	5.5	S R
13	20100213	02:34:28.86	−21.902	−174.767	11.0	6.0	S R
14	20100217	19:38:06.35	−29.756	−177.836	45.0	5.8	S R
15	20100219	11:13:19.81	−21.840	−175.115	10.0	5.4	S R
16	20100222	07:00:51.32	−23.626	−176.036	15.0	5.5	S R
17	20100903	16:35:47.77	−43.522	171.830	12.0	6.4	T
18	20110221	23:51:42.35	−43.583	172.680	5.9	6.1	T
19	20110418	13:03:02.73	−34.336	179.874	86.0	6.2	S R T

Note: Data is taken from the Earthquake Data Report provided by U.S.G.S.
S, events used for the derivation of station corrections; R, events for the analysis of a local reference velocity profile in the lower mantle; T, events used for analysis of the velocity structure at the base of the mantle and PcP, events used for PcP–P traveltime analysis.

vertical components of high-quality broad-band seismograms of 19 earthquakes that occurred in Vanuatu, Tonga, Fiji, South Fiji and New Zealand (Table 1).

The geographical distribution of hypocentres, stations and seismic rays are plotted in Fig. 1. The *P*-wave velocity perturbations at the base of the mantle using the GAP-P4 model (Obayashi *et al.* 2013) are presented for reference. As the location of the *P*-wave edge of the LLSVP varies from model to model, the zero contours around the concerned region are retrieved from several representative models (van der Hilst *et al.* 1997; Antolik *et al.* 2001; Karason & van der Hilst 2001; Becker & Boschi 2002). The ray portions that pass through the lowermost 100 km of the mantle are represented by blue lines, which perpendicularly intersect the zero contours of *P*-wave velocity perturbations at the base of the mantle. The approximate midpoints of *P*-waves are located within the inside margin of the LLSVP, and the reflection points of PcP waves from the Vanuatu event are near the zero contours. In the later sections, the survey area is split into five regions for convenience; numbers are plotted in the centre of each region in Fig. 1. Region 1 is covered by the ray paths from the Tonga-Fiji events where we infer a local reference velocity structure in the lowermost 600 km of the mantle except for the D'' region. Regions 2, 3 and 4 are covered by the ray paths from the South Fiji and New Zealand events where we examine the velocity structure at the base of the mantle. Region 5 is covered by the ray paths from the Vanuatu event where we examine the velocity structure at the base of the mantle using PcP–P traveltimes.

To measure relative *P*-wave traveltimes, seismograms including *P*-waves are converted to displacements (Fig. 2a) with sensor
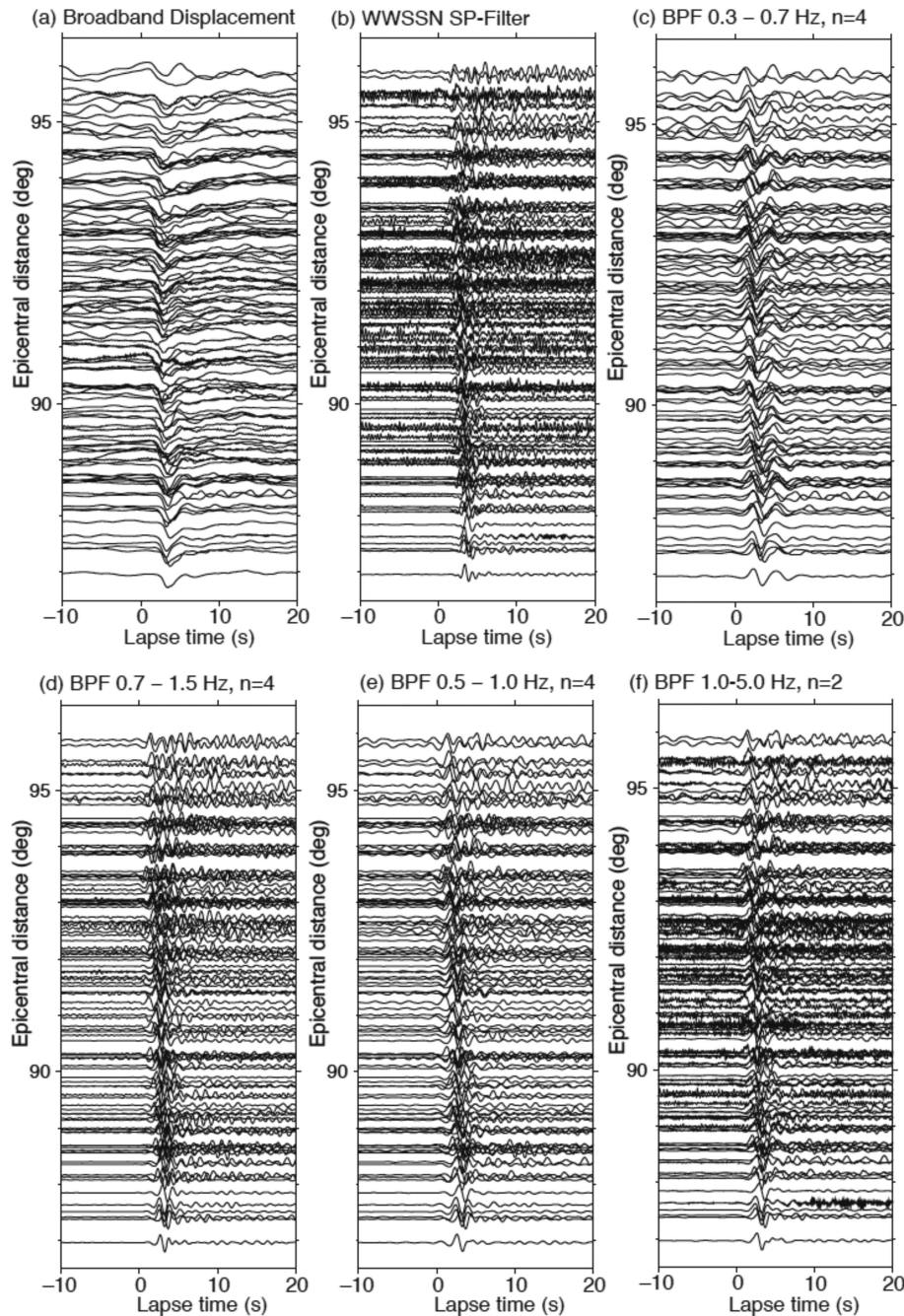

Figure 2. Example of processed seismograms for event No. 7, aligned with arrival times of *P*-waves calculated with PREM.

response corrections (NECESSArray mainly uses STS-2, CMG-3T and a few CMG-ESP). Seismograms are aligned on the arrival times of *P*-waves predicted by PREM (Dziewonski & Anderson 1981). To examine as fine structure as possible, we look for an observable highest frequency range by applying various filters, such as the WWSSN short-period filter (Fig. 2b), and bandpass filters with several combinations of cut-off frequencies and pole numbers (Figs 2c–f), and finally choose a zero-phase Butterworth filter with cut-off frequencies of 1 and 5 Hz and pole of 2 (Fig. 2f). The resulting predominant frequency is approximately 0.5 Hz with sufficient signal-to-noise ratio also for other events, which provides stable measurement of relative traveltimes. By comparison, waveforms with a predominant frequency of 1 Hz (Figs 2b and d) are characterized by coda waves at distances greater than approximately 94°. The amplitude of coda waves is compatible with that of the first arrivals and disturbs the traveltime measurement using waveform similarity. Waveforms with a predominant frequency of 0.5 Hz but with a narrow frequency band (Figs 2c and e) show a low signal-to-noise ratio at larger distances, and the resultant noise and signal are monochromatic. This makes it difficult to distinguish the signal and noise. However, a weak and relatively wide-range filter results in signal pulses comprising more multiple-frequency components than noises and is therefore suitable for waveform analysis (Fig. 2f).

For the measurement of PcP–P differential traveltimes, we employ displacement seismograms for which the filter with cut-off frequencies of 0.003 and 5 Hz is used. This filter is not described above because we did not find good PcP phases in short-period seismograms.

3 STATION CORRECTIONS AND REFERENCE VELOCITY STRUCTURE IN THE LOWER MANTLE ABOVE THE *D″* REGION

Relative traveltimes with respect to those predicted by PREM are measured from short period seismograms from 16 earthquakes occurring in Tonga, Fiji and South Fiji island regions (Table 1), using the adaptive stacking method (Rawlinson & Kennett 2004). The residuals are defined as fluctuations with respect to the median of the whole array for each event. The representative station anomaly is defined as the median value of the residuals at each station (Fig. 3a), the geographical distribution is shown in Fig. 3b. After subtraction of the station anomalies, ellipticity corrections (Kennett & Gudmundsson 1996) and distance corrections for the surface focus, we synthesize all the residuals to obtain a characteristic residual variation as a function of epicentral distance from 80° to 95°. Using the least squares method, traveltime residuals for the *i*th event and *j*th station, dT_{ij}, are fitted to two linear functions with different slopes, a_k,

$$dT_{ij} = a_k\Delta + b_i \quad (k = 1, \ 2; \ i = 1\ldots16), \tag{1}$$

where a_1 and a_2 are the traveltime slopes for epicentral distances Δ less and greater than 87°, respectively, and the offset adjustment, b_i, for the *i*th event. Traveltime residuals, dT_{ij}, after the offset adjustment show an inverted V-pattern with a maximum delay of approximately 0.3 s at 87° compared from a reference level at 80° and 95° (Fig. 4a). As shown in Fig. 4(b), the variation of the traveltime residuals depends on the deepest points of the seismic rays rather than their lateral location. Thus we interpret the residuals as a function of epicentral distance using the Herglotz–Wiechert inversion (Aki & Richards 2002), where the velocity structure >600 km
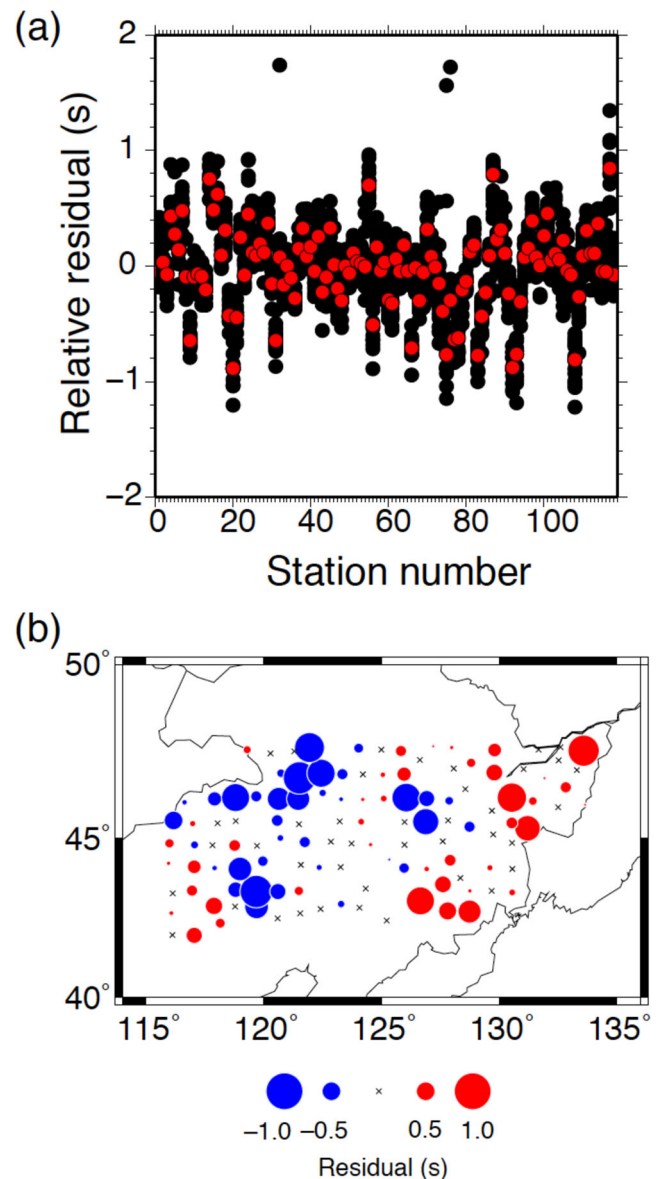

Figure 3. (a) Relative residuals of *P*-wave traveltimes to determine station corrections. Black circles are the residuals of *P*-wave traveltimes with respect to the median of the whole array for each event. Red circles are the median of the residuals at each station. (b) Geographical distribution of average *P*-wave residuals at each station.

above the CMB is assumed to be identical to PREM. This new velocity profile indicates that the difference of *P*-wave velocities from those of PREM gradually increase with depth and reach a maximum velocity reduction of 0.15 per cent at approximately 300 km above the CMB, and *P*-wave velocity gradually increases and approaches the PREM value (Fig. 4d). The thickness of a small velocity gradient layer at the base of the mantle is reduced to 130 km instead of the PREM value of 150 km.

For comparison, the radial *P*-wave velocity profiles of GAP-P4 (Obayashi *et al.* 2013) are plotted with the global average and at the following points (Fig. 1): No. 1 (12°N, 157°E), No. 2 (8°N, 153°E), No. 3 (2°N, 151°E), No. 4 (0°, 147°E) and No. 5 (17°N, 149°E). Because the global average velocity profile of GAP-P4 is slightly slower than that of PREM, all the velocity profiles in the five regions are slower than that derived above. However, the differences among the five velocity profiles from GAP-P4 are less
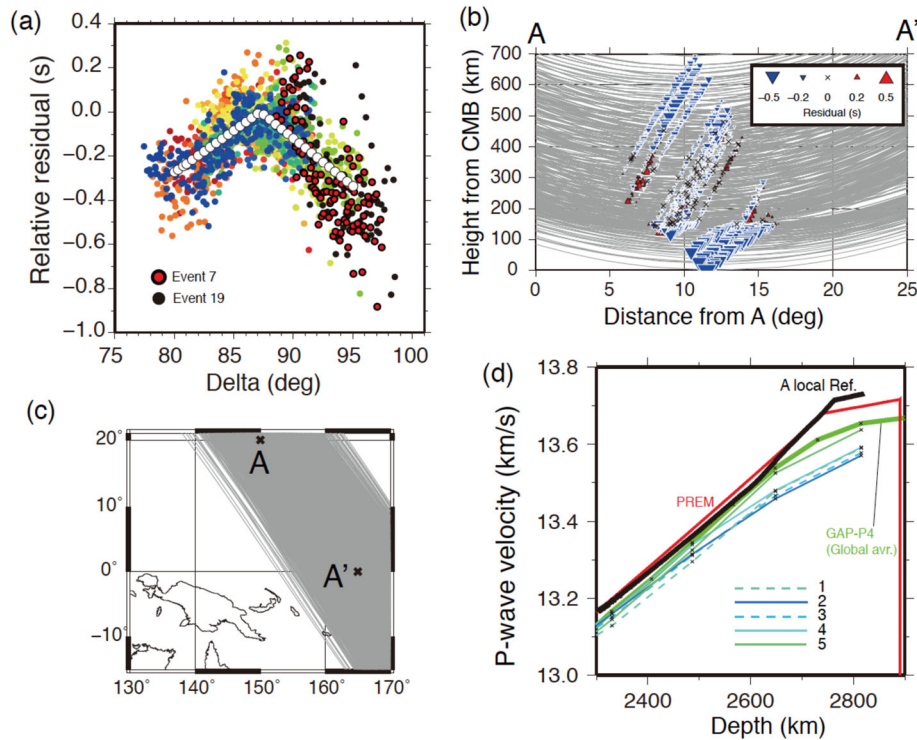
Figure 4. (a) A composite of traveltime residuals as a function of epicentral distance. The different coloured closed circles represent traveltime residuals from different events. The offsets are adjusted. Open circles represent the best-fitting traveltime residual using two linear lines. (b) The traveltime residuals with the offset adjustment projected at the deepest points of the seismic rays on the cross-section between A and A′ presented in (c). The grey lines are seismic rays. (d) The thick black, red and green lines are the *P*-wave velocity structures obtained in this study as a local reference, those of PREM and those of the global average of the GAP-P4 model (Obayashi *et al.* 2013), respectively. Thin and broken lines are *P*-wave velocity profiles at points 1–5 shown in Fig. 1.

than approximately 0.4 per cent except for that in the lowermost 300 km of the mantle. Furthermore, those at the points of Nos. 1–4 almost coincide with each other within approximately 0.2 per cent in the concerned depth range. These results suggest that the velocity structures in the mantle greater than approximately 100 km above the CMB by the ray paths from New Zealand and Vanuatu to NECESSArray (the Regions 3, 4 and 5), which are not inferred in this study, are not so much different from that inferred from the Fiji events (covering Regions 1 and 2). Thus, it is assumed that the *P*-wave velocity structures in the lower mantle, except for the lowermost approximately 100 km of the mantle beneath the entire study area, are represented by the local reference profile obtained above.

4 VELOCITY STRUCTURE AT THE BASE OF THE MANTLE FROM RELATIVE TRAVELTIMES OF *P*-WAVES

In this section, we examine the *P*-wave velocity structure in the lowermost ∼100 km of the mantle using the traveltime data from the South Fiji events (Nos. 7 and 19). Also, the traveltime residuals from the New Zealand events (Nos. 17 and 18) are examined and measured by the adaptive stacking method, and station and ellipticity corrections are applied. Fig. 5 shows the geographical distribution of the *P*-wave traveltime residuals at the deepest points. As noted in the previous section, we do not have sufficient data to examine the velocity structure in the lowermost 100 km of the mantle beneath Region 1. Instead we focus on Regions 2, 3 and 4, where many ray paths pass through the lowermost mantle. The residuals in the middle area marked as Region 2, which comprise the composite
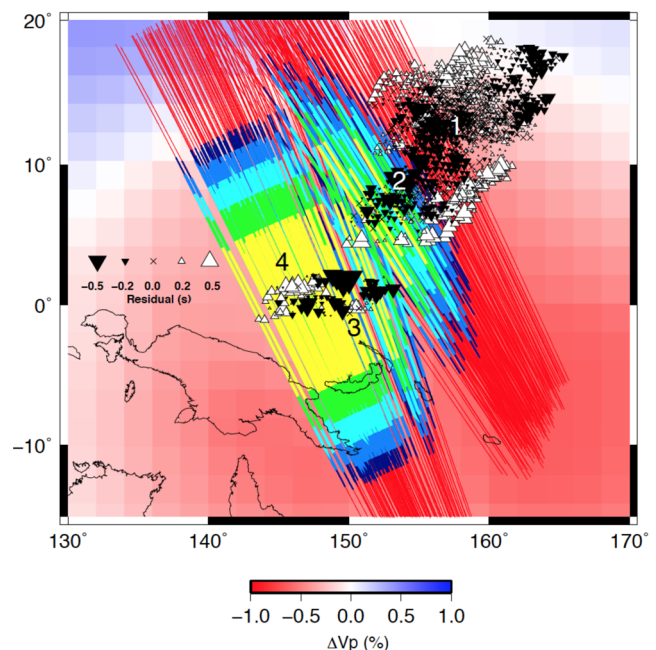

Figure 5. Geographical distribution of the traveltime residuals represented by white triangles (positive) and black inverse triangles (negative). Seismic rays paths passing through the lowermost 300 km of the mantle are displayed, which are calculated with PREM. Red, blue, light blue, green and yellow lines represent seismic rays passing through the lowermost 300, 100, 60, 40 and 20 km of the mantle, respectively.

residuals from events 7 and 19, vary from positive in the southeast to negative in the northwest. The residuals in Regions 3 and 4, which comprise the composite residuals from events 17 and 18, are dominated by negative and positive residuals, respectively.

Regarding the events that are examined here, Fig. 5 shows ray portions calculated for PREM, within the lowermost 300 km of the mantle. They indicate that only a few seismic ray paths pass through in the lowermost 20 km of the mantle in Region 2. However, if the velocity gradient in the lowermost mantle is 1.5×10^{-3} s^{-1} instead of the flat velocity gradient in PREM, which is a plausible value to be discussed later, *P*-wave seismic rays from an earthquake with a focal depth of 500 km graze the CMB at a distance of approximately 90°. In Fig. 4a, the residuals from events 7 and 19 are represented by red and black circles, of which slope as a function of epicentral distance is steeper than the obtained linear function at distances greater than 87°. Taking a closer look, we plot the traveltime residuals with epicentral distances up to 96° for event 7 and up to 98° for event 19 in Figs 6(a) and (b), respectively. Here, the relative traveltime residuals are applied for ellipticity and station corrections, but not distance correction due to focal depths. The residuals gradually reduce with increasing distance up to approximately 92°–93° and become almost flat at larger distances. Next, the relative traveltimes obtained from the two New Zealand events are plotted (Nos. 17 and 18) in Figs 6c and d. The residuals in Regions 3 and 4 roughly indicate the patterns of uniform decrease and uniform increase, respectively.

To explain these observations, forward modelling with the reflectivity method (Kennett 1988) is conducted because the traveltime analysis with the ray theory is invalid in the concerned distance range. A starting *P*-wave velocity model is constructed with a stack of layers with a typical thickness of 1 km, interpolated from the local reference velocity model obtained in the previous section. The Earth-flattening approximation (Müller 1985) is then applied to the model. *S*-wave velocity, density and *Q* structures are taken from PREM. First, we modify the *P*-wave velocity gradient in the lowermost 130 km of the mantle to account for the steep negative slope of the traveltime residuals in the shorter distance range, especially for events 7 and 19 (Figs 6a and b). For this, we vary the velocity increase from 0.10 to 0.50 km s^{-1} with increments of 0.02 km s^{-1} at the bottom of the mantle. To further explain the observed residuals, we introduce a basal layer whose thickness is 10, 20, 30, 40, 50, 60, 80, 100 and 120 km and whose velocity change varies from -1.5 to 0.9 km s^{-1} with an interval of 0.1 km s^{-1} rather than introducing velocity gradients for simplicity. All considered velocity structures are plotted with blue lines in Fig. 7. So far, we have tested the 3024, 3024, 3570 and 3570 models shown in Figs 7(a)–(d), respectively.

Next, we synthesize vertical broad-band displacement seismograms with a sampling interval of 0.05 s and frequency range of 0.05–5 Hz and apply the same band-pass filter, as in the observations. The stations numbers and focal depths depend on the events. As the hypocentres of the two New Zealand events are very close to each other, we adopt the hypocentre information of the larger earthquake (event 17 in Table 1). After aligning the synthetic waveforms on the *P*-wave arrival times predicted by PREM, the residuals of the relative traveltimes are measured by the adaptive stacking method, as in the observed waveforms. Fig. 8 shows the comparison of the
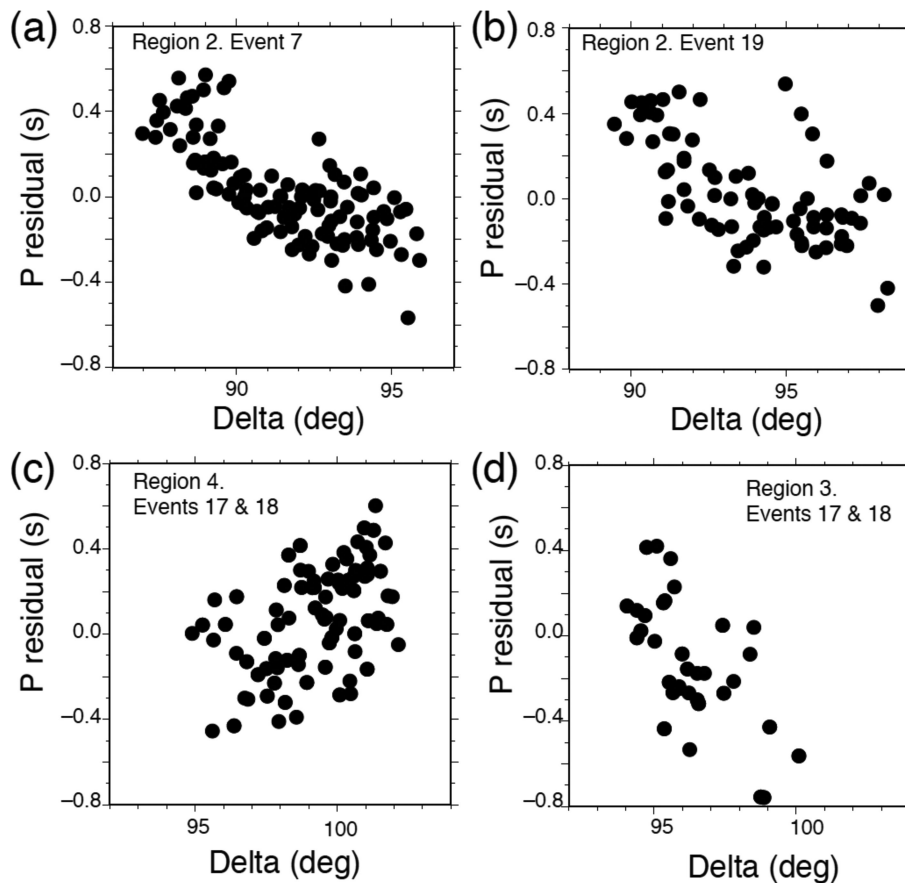

Figure 6. Relative traveltime residuals as a function of epicentral distance for (a) event 7 sampling Region 2, (b) event 19 sampling Region 2, (c) events 17 and 18 sampling Region 4 and (d) events 17 and 18 sampling Region 3.
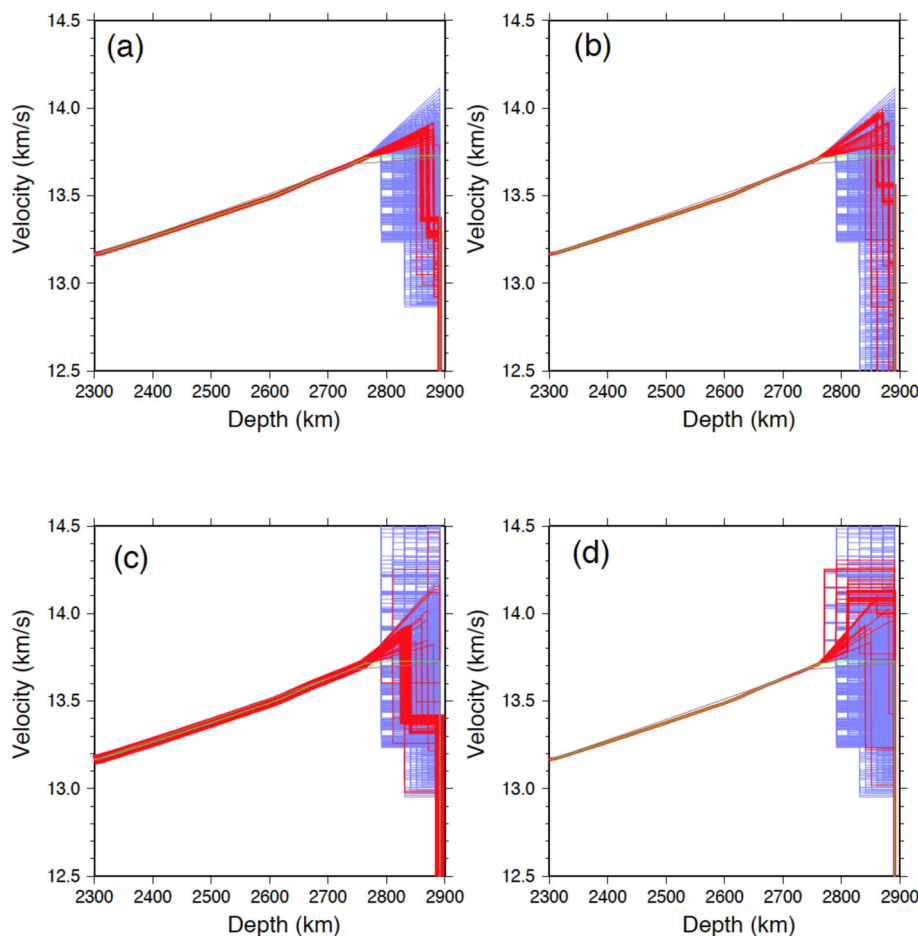
Figure 7. *P*-wave velocity structures in the lowermost 600 km of the mantle examined by forward modelling for (a) event 7 sampling in Region 2, (b) event 19 sampling in Region 2, (c) events 17 and 18 sampling in Region 4 and (d) events 17 and 18 sampling in Region 3. Thin blue lines represent all the examined structures; thick red lines are the best-fit ones. Thin green and black lines are the reference model and PREM, respectively, for comparison.

observed relative traveltime residuals with those obtained from the synthetics. To compare the variation of the relative residuals as a function of epicentral distance, we take bin-averages for a $\pm 1°$ window with an increment of $0.5°$ and adjust the average of the traveltime residuals from both the observation and synthetic waveforms and search for the best velocity model using the least squares. To estimate the uncertainty of the parameters in the inferred *P*-wave velocity structures, the Bootstrap method is adopted (Efron & Tibshirani 1993). One hundred artificial data sets are produced by uniform random sampling with the permission of duplication from the original data.

In Fig. 7, the best *P*-wave velocity model for each artificial dataset is highlighted by a red line. The distributions of the inferred parameters are shown in Fig. 9. The data from event 7 (the South Fiji event), that samples Region 2, is explained by a slow basal layer with a 3.6 $\pm$ 1 per cent (13.23 $\pm$ 0.14 km s^{-1}) slower *P*-wave velocity at the CMB than PREM and an 18.6 $\pm$ 7.9 km thickness. The velocity gradient above the basal low-velocity layer is $(1.4 \pm 0.2) \times 10^{-3}$ s^{-1} (0.18 ± 0.03 km s^{-1}/130 km; Fig. 9a). The data from event 19 (the South Fiji Event), that also samples Region 2, is explained by a slow basal layer with a 4.8 $\pm$ 3.1 per cent (13.04 $\pm$ 0.43 km s^{-1}) slower *P*-wave velocity at the CMB than PREM and a 22.6 $\pm$ 12.0 km thickness. The velocity gradient above the basal low-velocity layer is $(1.7 \pm 0.5) \times 10^{-3}$ s^{-1} (0.22 ± 0.07 km s^{-1}/130 km; Fig. 9b). Although the uncertainties of the parameters obtained from event

19 are much larger than those obtained from event 7 because of data scatter, we can conclude that Region 2 is characterized by a *P*-wave velocity structure with a basal layer of thickness of approximately 20 km, velocity reduction of 3 –5 per cent and positive velocity gradient above the basal low-velocity layer. In the case of the New Zealand events, the traveltime variation in Region 4 can be explained by a low-velocity layer at the base of the mantle, velocity reduction of 2.2 $\pm$ 1.5 per cent (13.40 $\pm$ 0.2 km s^{-1}) and thickness of 54.6 $\pm$ 14.9 km (Fig. 9c). Region 3 can be explained by a structure with a basal layer with a velocity increase of 2.4 $\pm$ 1.9 per cent (14.03 $\pm$ 0.26 km s^{-1}) and 76 $\pm$ 25 km thickness (Fig. 9d).

In the waveforms synthesized with the typical best-fitting model for event 7 (*P*-wave velocity at the CMB is 13.28 km s^{-1}, the LVZ thickness is 20 km, the velocity gradient above the LVZ is 1.5 $\times$ 10^{-3} s^{-1}; see Fig. 7a), later phases originated from the thin low velocity layer can be identified in the short-period seismograms at larger distances rather than broad-band records as shown in Fig. 10(a). Looking at the observed short-period seismograms in consideration of such later phases, we can find some corresponding arrivals. However, these are incoherent and lasting a bit longer than those in the synthetic, suggesting the existence of complexity at the base of the mantle. On the other hand, in the observed *P*-waveforms passing through Region 3, we did not identify any phases probably originated from the assumed discontinuity because of a complicated source time function and contamination of the depth phases. Since a
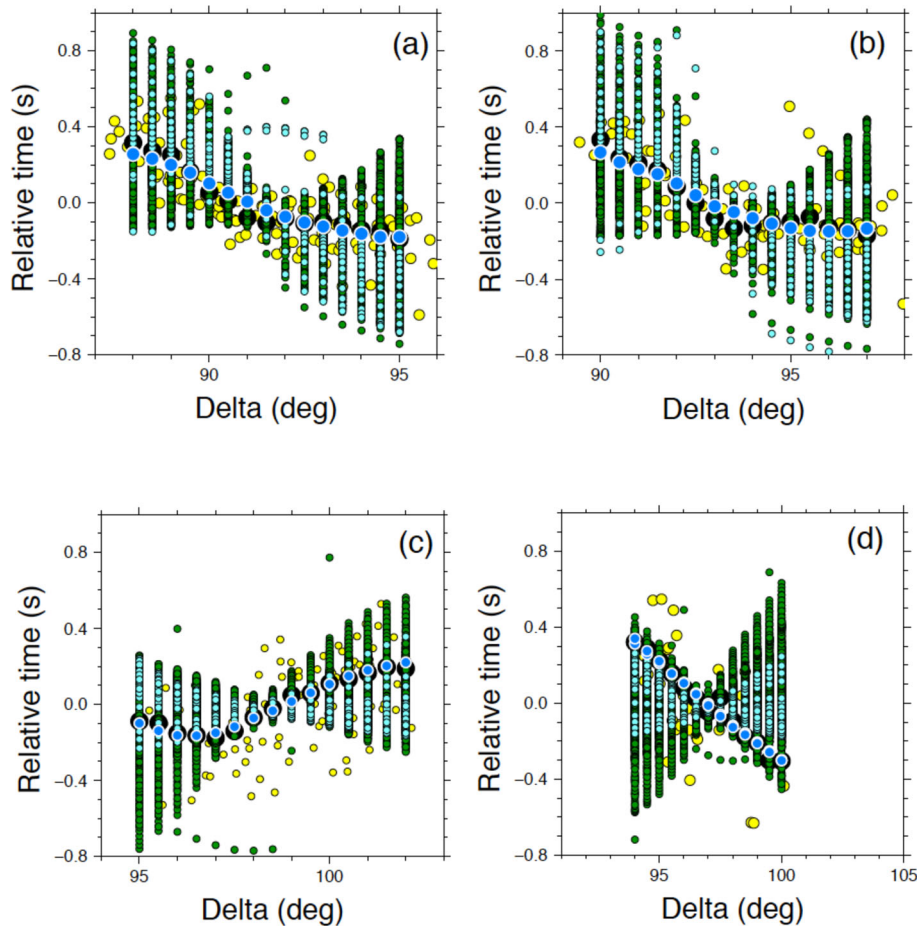
Figure 8. Relative traveltime residuals for (a) event 7 sampling in Region 2, (b) event 19 sampling in Region 2, (c) events 17 and 18 sampling in Region 4, (d) events 17 and 18 sampling in Region 3. The small yellow and large black circles are the observed and bin-averaged residuals, respectively. The small light blue and green circles are the theoretical residuals for various velocity gradients and additional basal layers, respectively. The large blue circles represent the residuals from the best-fitting models.

simple positive velocity gradient was not enough to explain the traveltime variation, and the largest velocity gradient considered here resulted in strong waveform distortion, we introduced a discontinuous high-velocity layer for Region 3. We find later phases owing to multipathing in the shorter distances in the synthetic seismograms for the best-fitting velocity model, which are not confirmed by the observation.

5 VELOCITY STRUCTURE AT THE BASE OF THE MANTLE FROM PcP–P TRAVELTIMES

Phase weighted stacking (Schimmel & Paulssen 1997) is applied to the waveform data from event 11 to search for additional phases reflected from discontinuities in the lowermost mantle beneath Region 5. However, we did not find any significant signals that suggest the existence of discontinuities in the D'' region. Furthermore, PcP–P data has no depth resolution. Thus, we only consider the variations of the velocity gradient in the lowermost 130 km of the mantle, as shown in Fig. 11a. PcP–P traveltimes are measured using the cross-correlation method on the observed seismogram, which are then compared with those measured on seismograms synthesized by the reflectivity method. The PcP–P residuals for the local reference model (the green line in Fig. 11a) are plotted on the map (Fig. 11b) corresponding to Region 5 (Fig. 1), where the average of

the residuals is −0.4 s, suggesting the existence of a high-velocity region at the base of the mantle. As a result of the forward modelling, we find that the velocity structure with a velocity gradient of 1.5×10^{-3} s^{-1} (0.20 km s^{-1}/130 km) represented by the thick red line in Fig. 11(a) is best among the considered models. The average of the PcP–P residuals is 0.0 s with a standard deviation of 0.3 s (Fig. 11c).

Because Region 5 is in very close proximity to Region 2, the observed PcP–P traveltimes can be compared with those measured on the seismograms synthesized with the velocity structure with a basal low-velocity layer. The PcP–P traveltimes are sensitive to the low-velocity layer, where the residual is −0.64 s for a 20-km-thick layer with a velocity reduction of 3 per cent and −0.80 s for a 10-km-thick layer with a velocity reduction of 6 per cent. This finding suggests that the above two velocity structures are much slower than a true one. Furthermore, such thin low-velocity layers can create a larger PcP phase and a precursory signal to PcP, as observed by Mori & Helmberger (1995), beneath the central Pacific (Figs 12c and d). However, we do not find such a large PcP and a precursory peak in the vespagram and the stacked trace from observed seismograms (Fig. 12a) and in those from synthetic waveforms for the best-fitting velocity structure (Fig. 11a) that does not have a thin low-velocity layer (Fig. 12b). Thus, we can rule out the possibility that a low-velocity layer with thickness greater than or equal to 10 km exists in Region 5.
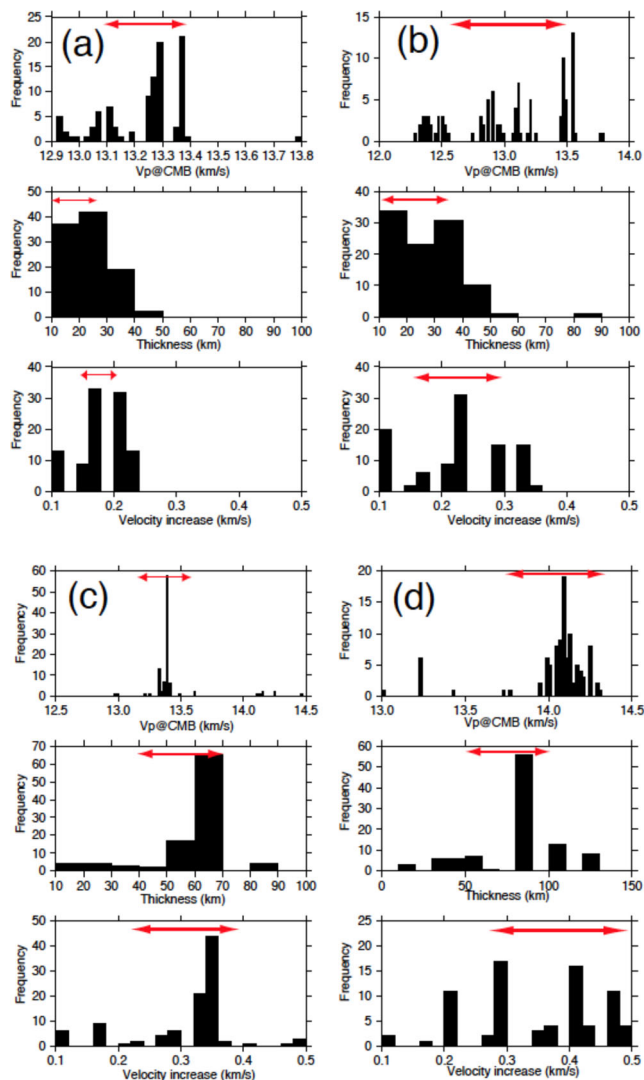
Figure 9. Histograms of inferred parameters, *P*-wave velocity at the CMB, thickness of the basal layer and velocity increase in the lowermost 130 km of the mantle for (a) Region 2 by event 7, (b) Region 2 by event 19, (c) Region 4 and (d) Region 3. The red arrows show the uncertainties ($\pm 1\sigma$) for the estimated parameters.

6 DISCUSSION

At the base of the mantle, thin low-velocity zones (LVZs) are detected in Regions 2 and 4 (Figs 1 and 5), where the *P*-wave velocities are 2–5 per cent slower than that of PREM. The magnitudes of the velocity reductions are smaller than those in the ULVZs, but larger than those seen in a typical low-velocity region in global tomographies. The LVZs are located near the western *P*-waves edge of the Pacific LLSVP (Fig. 1). These observational characteristics, especially the smaller velocity reduction, may be explained by a thermal anomaly on the edge of a metastable superplume having a bulk modulus 6 per cent higher and density 2 per cent higher than the ambient mantle (Sun *et al.* 2007). However, the velocity reductions in the LVZs in this study are consistent with those in a so-called weak ULVZ (Hutko *et al.* 2009). Furthermore, if we could analyse higher frequency contents than 0.5 Hz at which we analyse in this study, thinner and larger velocity reductions might be detected as per Xu & Koper (2009), who find that a 6 per cent *P*-wave velocity reduction observed at 2 Hz is only observed as only a 3 per cent
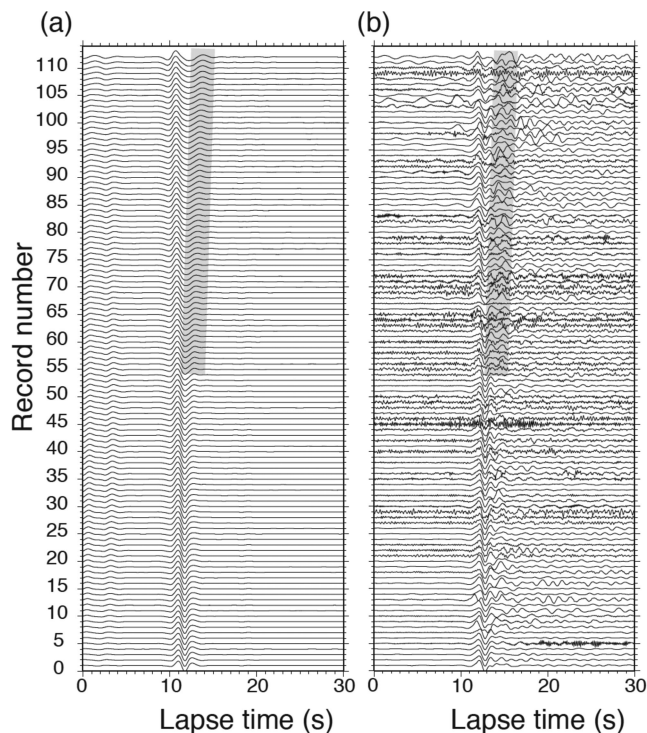

Figure 10. Record sections aligned in the order of distance. The lapse times are adjusted for the *P*-wave arrivals. (a) Synthetic seismograms calculated from the typical best-fitting model for event 7 (*P*-wave velocity at the CMB is 13.28 km s^{-1}, the thickness of the LVZ is 20 km, the velocity gradient above the LVZ is 1.5×10^{-3} s^{-1}, see Fig. 7a). The hatched area indicates later phases from the thin low velocity layer. (b) Observed seismograms for event 7. The hatched area corresponds to that shown in (a).

reduction at 1 Hz. Thus, in the following, we discuss the LVZs along the similar lines of interpretation as the ULVZs.

Although the strict definition of lateral spatial extents in the examined region is problematic, through a visual inspection on Fig. 5 the extents of the LVZs in this study can be roughly estimated to be several hundred kilometres at the CMB. This scale is comparable with ULVZs beneath the Philippines (Idehara *et al.* 2007; Idehara 2011), larger than small ULVZs beneath the east of Australia (Rost *et al.* 2010a), and smaller than Mega ULVZs beneath the southern and central Pacific (Cottaar & Romanowicz 2012; Thorne *et al.* 2013). Therefore, regarding lateral extent, we can conclude that the LVZs detected in this study are of medium size.

Some ULVZs that are thought to be originated from partial melt (Williams & Garnero 1996) would be expected to be located near the margin of the LLSVP (Garnero & McNamara 2008; Hernlund & Jellinek 2010; McNamara *et al.* 2010), where the highest temperature anomaly is reproduced by numerical simulations for thermochemical piles (Tan *et al.* 2011). Actually, numerous seismic studies have supported the hypothesis through the observations of PcP and ScP phases, by which the ULVZs with $d\ln Vp/d\ln Vs = 1/3$ and high density are detected near the margin of the LLSVP (Rost *et al.* 2005, 2010a) and no ULVZ exists outside the LLSVP (Vidale & Benz 1992; Castle & van der Hilst 2000; Persh *et al.* 2001; Rost *et al.* 2010b). Rost *et al.* (2005) considered that a spot-like ULVZ observed beneath the east of Australia, with varying thickness at the base of the mantle, is a possible sign of a mantle plume source. Regarding the LVZs in this study, since the analysis of shear wave velocity structure by using the NECESSArray data is not completed, we tentatively compare our results with the shear wave
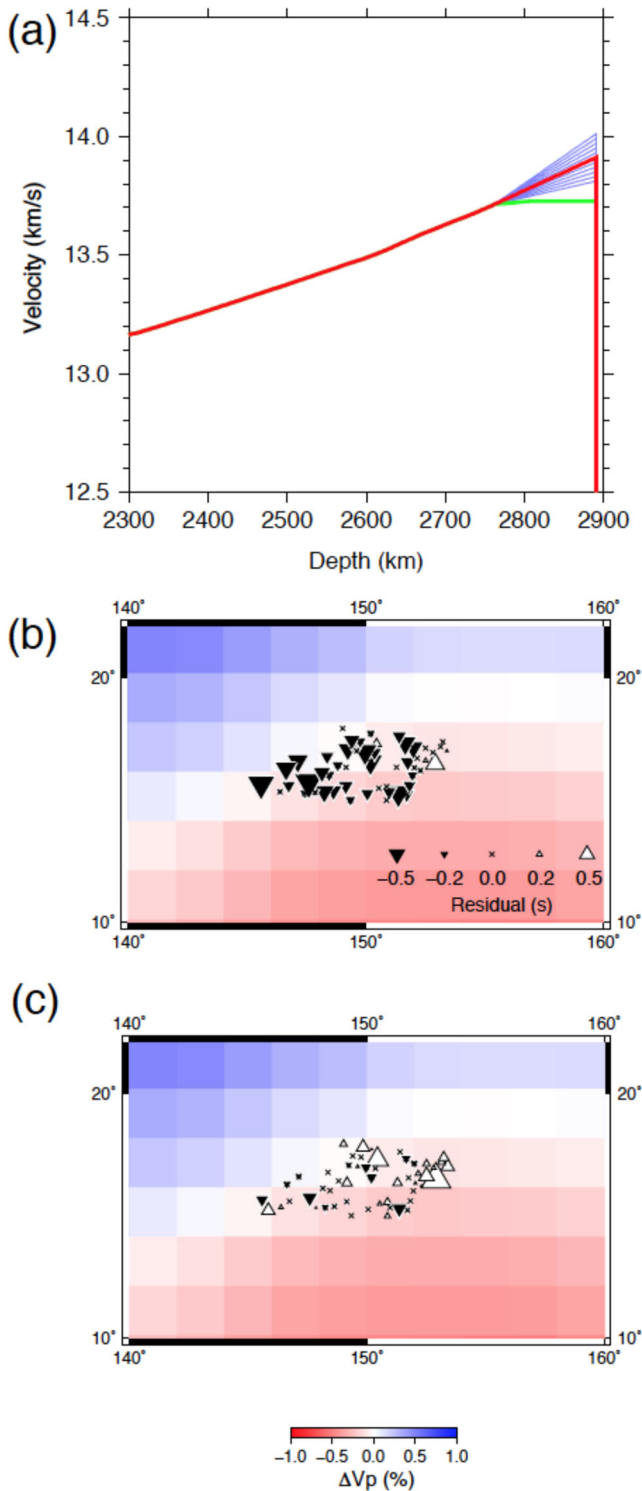
Figure 11. (a) *P*-wave velocity structures in the lowermost 600 km of the mantle examined by forward modelling. Thin blue lines represent all the examined structures; thick red lines are the best-fit ones. The green line is the local reference model for comparison. (b) Geographical distribution of PcP–P traveltime residuals for the local reference model (green line in Fig. 11a). The background colour shows the *P*-wave velocity perturbation from the GAP-P4 model (Obayashi *et al.* 2013). (c) Same as (b) except for the best-fitting model (thick red line in Fig. 11a).

velocity structure observed by He *et al.* (2006) and He & Wen (2009) beneath near Region 2. They detected a shear wave ULVZ with a thickness of 30–100 km and a reduction of 10–13 per cent at the base of the mantle and dln*Vp*/dln*Vs* can be obtained to be approximately 1/3–1/2 as a very rough estimation. However, the thicknesses of our LVZs and their ULVZ in the later work are completely different, the detailed geographical comparison is incomplete, and the estimated dln*Vp*/dln*Vs* has a large uncertainty. Therefore the existence of melt inclusions in the LVZ is inconclusive.

Although the hypothesis of ULVZ caused by partial melt at the edge of LLVZ is still valid, the number of studies detecting ULVZs in exceptional regions (Mori & Helmberger 1995; Revenaugh & Meyer 1997; Havens & Revenaugh 2001; Idehara *et al.* 2007; Xu & Koper 2009; Idehara 2011) and/or with a properties of dln*Vp*/dln*Vs* ≠ 1/3 (Hutko *et al.* 2009) have increased. Furthermore, the many other origins of the ULVZ have been discussed, for example iron-rich magnesium silicate (Fe, Mg)SiO$_3$ (Mao *et al.* 2005) and its melt (Nomura *et al.* 2011) and iron-rich oxide (Mg, Fe)O (Wicks *et al.* 2010; Bower *et al.* 2011; Sun *et al.* 2013), which can be come from the interaction at the CMB (Knittle & Jeanloz 1989) or a remnant of a basal magma ocean in the early Earth (Labrosse *et al.* 2007) or the segregation from a subducted slab (Dobson & Brodholt 2005).

Some recent observations have detected ULVZs around a high-velocity zone (HVZ) that can be interpreted to be a subducted slab (Hutko *et al.* 2009; Yao & Wen 2014). Numerical simulations confirm that the distribution of dense ULVZs are affected by a mantle downwelling pattern and predominantly located at the boundary of a large-scale chemical reservoir, possibly corresponding to LLSVPs (McNamara *et al.* 2010). This result suggests that a subducted slab may shift areas of ULVZs. Furthermore, the volume of subducted material during past 130 Ma is largest in Southeast Asia (Wen & Anderson 1995). Interaction between the subducted slab and the LLSVP in western Pacific would be more active than that in northern and eastern Pacific where Frost & Rost (2014) examined the boundary of the Pacific LLSVP for *P*-waves. Therefore, it is necessary to consider not only LVZs but also to HVZs in Region 3 and a positive velocity gradient without an LVZ in Region 5.

LVZs in Regions 2 and 4 are decoupled by an HVZ in Region 3 of the LLSVP (Fig. 13a). The thickness of the high-velocity layer in Region 3 is approximately 80 km and velocity increase is 2.4 per cent, consistent with typical values of *P*-wave velocity discontinuities in the lowermost mantle; for example, a thickness of 70–350 km and velocity increase of 0.5–3 per cent (Wysession *et al.* 1998). However, Weber & Körnig (1992) analysed the bulletin of International Seismological Centre and could not detect any significant arrivals due to *P*-wave velocity discontinuities in the lowermost mantle beneath the western Pacific. Although Yamada and Nakanishi (1996, 1998) exceptionally reported a discontinuity located in the middle of the no-detection region mapped by Weber & Körnig (1992), many other studies have not supported the existence of such an HVZ (Shibutani *et al.* 1993; Kito & Kruger 2001; Kito *et al.* 2004). Thus, the HVZ in Region 3 could be an exceptional structure of the LLSVP. Conversely, the LVZ of Region 2 is located in southeast of the region with a positive velocity gradient in Region 5 where the approximate border of the LLSVP lies (Fig. 13b). The feature along this cross-section is qualitatively similar to the shear wave velocity structure obtained by He & Wen (2009), who demonstrated the existence of HVZs located above the ULVZ and in the northwest of the ULVZ, where the *S*-wave velocity gradient in their HVZs is negative. This discrepancy of the velocity gradients of *P*- and *S*-waves is similar to the observation in the northern edge
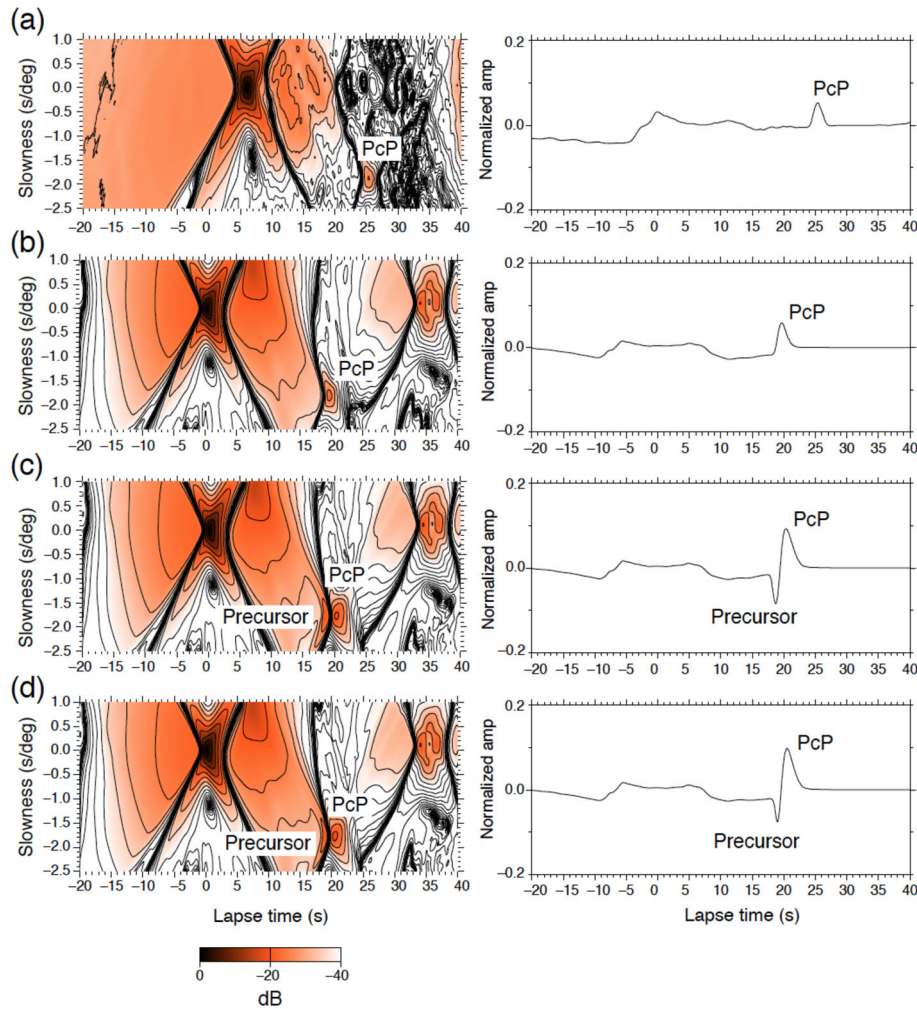
Figure 12. Left-hand side: Vespagrams constructed by the phase-weighted stack with a power index of 2 for (a) the observed seismograms, (b) synthetic seismograms with the best-fitting velocity models shown in Fig. 11a (positive velocity gradient), (c) those with the basal low-velocity layer with a 20 km thickness and velocity reduction of 3 per cent and (d) those with the basal low-velocity layer with a 10 km thickness and velocity reduction of 6 per cent. Amplitude colour scale is decibels (dB). Right-hand side: Stacked traces tuned on PcP phases.

of LLSVP (Russell *et al.* 2001). However, we should note that the comparison here is tentative and further confirmation is required.

Interestingly, high- and low-velocity layers at the CMB in Regions 2, 3, 4 and 5 alternatively appear with spatial distances of several hundred kilometres. Such a rapid and small-scale lateral variation of radial velocity structures can be detected since we deploy a dense and large aperture seismic array. Differences between *P*-wave velocities at the base of the mantle between Regions 2 and 3 and between Regions 4 and 3 are 4–7 per cent. A difference between Regions 5 and 2 is approximately 5 per cent. If we assume that velocity variations originated only from temperature differences, and using a derivative coefficient of the order of 10^{-5} K^{-1} (Oganov *et al.* 2001; Trampert *et al.* 2001; Stacey & Davis 2004), we calculate that the temperature differences would reach several thousand degrees. As this estimate of temperature difference is highly unlikely, some other mechanism such as the existence of partial melts (Williams & Garnero 1996), compositional differences (Mao *et al.* 2005; Wicks *et al.* 2010) or some combination of the two (Nomura *et al.* 2011) is probable. The feature that a small-scale HVZ intersects relatively low velocity regions is similar to that discovered beneath the northwest Pacific by Xu & Koper (2009), who used a small-aperture array at Yellowknife, Canada to measure the slowness of Pdiff. However,

this rapid variation is observed near the boundary of the anomaly in perovskite contents found by Trampert *et al.* (2004), not in the seismic positive and negative velocity anomalies, whereas our sampling region is located near the boundary of seismic velocity anomalies and in the deep inside of the perovskite enriched region by Trampert *et al.* (2004).

7 CONCLUSIONS

P-wave velocity variations at the base of the mantle are detected beneath the western Pacific at the western edge of the LLSVP. These observations are made through the analysis of relative *P*-wave traveltime variations observed near the core shadow zone by NECESSArray, as well as PcP–P traveltime residuals. Inside the LLSVP margin, a high-velocity layer, approximately 80 km thick and a 2 per cent velocity increase, interrupts basal low-velocity layers with thickness of 20–50 km and velocity reductions of 2–5 per cent. At the boundary of the LLSVP, a simple positive velocity gradient, without any basal layers at the base of the mantle, is located to the northwest of the thin low-velocity layer. Differences between the high and low velocities at the CMB are 4–7 per cent with spatial distances of approximately several hundred kilometres.
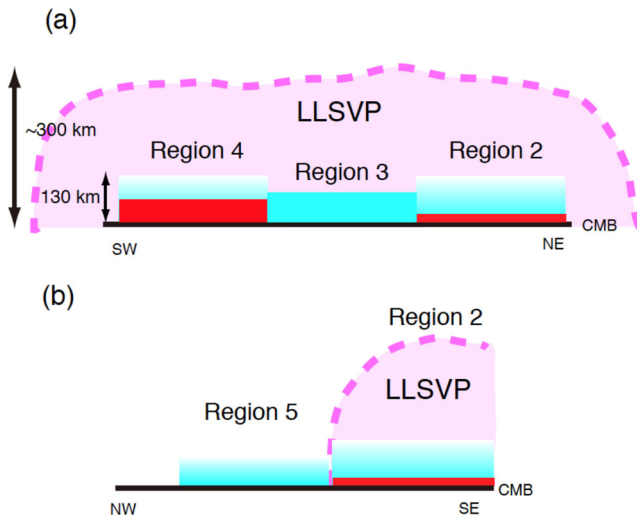
Figure 13. Schematic images for the inferred *P*-wave velocity structures (a) along the edge of the LLSVP roughly from the southwest to northeast and (b) on the cross-section subparallel to the ray paths from the South Fiji and Vanuatu events (SE) to stations (NW) (Fig. 1). The LLSVP is inferred from global tomography, whose height is approximately 300 km. The red and blue boxes represent low- and high-velocity regions, respectively. The boxes with white to blue gradation represent a positive velocity gradient. The Region numbers correspond to those found in Figs 1 and 5.

Such rapid and large variations cannot be explained by the thermal origin exclusively. These complicated structures suggest the occurrence of a wealth of thermochemical processes at the base of the mantle near the edge of the Pacific LLSVP.

REFERENCES

Aki, K. & Richards, P.G., 2002. *Quantitative Seismology*, 2nd edn, University Science Book.

Antolik, M., Ekstrom, G., Dziewonski, A.M., Gu, Y.J., Pan, J. & Boschi, L., 2001. A new joint P and S velocity model of the mantle parameterized in cubic B-splines, in *Proceedings of the 22nd Annual DoD/DOE Seismic Research Symposium: Planning for Verification of Compliance with the Comprehensive Nuclear-Test-Ban Treaty (CTBT)*, Vol. II, New Orleans, LA.

Becker, T.W. & Boschi, L., 2002. A comparison of tomographic and geodynamic mantle models, *Geochem. Geophys. Geosys.*, **3**(1), 1003, doi:10.1029/2001GC000168.

Boschi, L., Becker, T.W. & Steinberger, B., 2007. Mantle plumes: dynamic models and seismic images, *Geochem. Geophys. Geosys.*, **8**, Q10006, doi:10.1029/2007GC001733.

Boschi, L., Becker, T.W. & Steinberger, B., 2008. On the statistical significance of correlations between synthetic mantle plumes and tomographic models, *Phys. Earth planet. Inter.*, **167**, 230–238.

Bower, D.J., Wicks, J.K., Gurnis, M. & Jackson, J.M., 2011. A geodynamic and mineral physics model of a solid-state ultralow-velocity zone, *Earth planet. Sci. Lett.*, **303**, 192–202.

Burke, K., Steinberger, B., Torsvik, T.H. & Smethurst, M., 2008. Plume generation zones at the margins of Large Low Shear Velocity Provinces on the core-mantle boundary, *Earth planet. Sci. Lett.*, **265**, 49–60.

Castle, J.C. & van der Hilst, R.D., 2000. The core-mantle boundary under the Gulf of Alaska: no ULVZ for shear waves, *Earth planet. Sci. Lett.*, **176**, 311–321.

Cottaar, S. & Romanowicz, B., 2012. An unusually large ULVZ at the base of the mantle near Hawaii, *Earth planet. Sci. Lett.*, **355–356**, 213–222.

Dobson, D.P. & Brodholt, J., 2005. Subducted banded iron formations as a source of ultralow-velocity zones at the core-mantle boundary, *Nature*, **434**, 371–374.

Dziewonski, A.M., 1984. Mapping the lower mantle: determination of lateral heterogeneity in P velocity up to degree and order 6, *J. geophys. Res.*, **89**, 5929–5952.

Dziewonski, A.M. & Anderson, D.L., 1981. Preliminary reference Earth model, *Phys. Earth planet. Inter.*, **25**, 297–356.

Efron, B. & Tibshirani, R.J., 1993. *An Introduction to the Bootstrap*, Chapman and Hall/CRC.

Frost, D.A. & Rost, S., 2014. The P-wave boundary of the Large-Low Shear Velocity Province beneath the Pacific, *Earth planet. Sci. Lett.*, **403**, 380–392.

Garnero, E.J. & McNamara, A.K., 2008. Structure and dynamics of Earth's lower mantle, *Science*, **320**, 626–628.

Havens, E. & Revenaugh, J., 2001. A broadband seismic study of the lowermost mantle beneath Mexico: constraints on ultralow velocity zone elasticity and density, *J. geophys. Res.*, **106**, 30 809–30 820.

He, Y. & Wen, L., 2009. Structural features and shear-velocity structure of the "Pacific Anomaly", *J. geophys. Res.*, **114**, B02309, doi:10.1029/2008JB005814.

He, Y., Wen, L. & Zheng, T., 2006. Geographic boundary and shear wave velocity structure of the "Pacific anomaly" near the core-mantle boundary beneath western Pacific, *Earth planet. Sci. Lett.*, **244**, 302–314.

Hernlund, J.W. & Jellinek, A.M., 2010. Dynamics and structure of a stirred partially molten ultralow-velocity zone, *Earth planet. Sci. Lett.*, **296**, 1–8.

Houser, C., Masters, G., Shearer, P. & Laske, G., 2008. Shear and compressional velocity models of the mantle from cluster analysis of long-period waveforms, *Geophys. J. Int.*, **174**, 195–212.

Hutko, A.R., Lay, T. & Revenaugh, J., 2009. Localized double-array stacking analysis of PcP: D″ and ULVZ structure beneath the Cocos plate, Mexico, central Pacific, and north Pacific, *Phys. Earth planet. Inter.*, **173**, 60–74.

Idehara, K., 2011. Structural heterogeneity of an ultra-low-velocity zone beneath the Philippine Islands: implications for core-mantle chemical interactions induced by massive partial melting at the bottom of the mantle, *Phys. Earth planet. Inter.*, **184**, 80–90.

Idehara, K., Yamada, A. & Zhao, D., 2007. Seismological constraints on the ultralow velocity zones in the lowermost mantle from core-reflected waves, *Phys. Earth planet. Inter.*, **165**, 25–46.

Idehara, K., Tanaka, S. & Takeuchi, N., 2013. High-velocity anomaly adjacent to the western edge of the Pacific low-velocity province, *Geophys. J. Int.*, **192**, 1–6.

Inoue, H., Fukao, Y., Tanabe, K. & Ogata, Y., 1990. Whole manle P-wave travel time tomography, *Phys. Earth planet. Inter.*, **59**, 294–328.

Karason, H. & van der Hilst, R.D., 2001. Tomographic imaging of the lowermost mantle with differential times of refracted and diffracted core phases (PKP, Pdifff), *J. geophys. Res.*, **106**, 6569–6588.

Kennett, B.L.N., 1988. Systematic approximations to the seismic wavefield, in *Seismological Algorithms: Computational Methods and Computer Programs*, pp. 237–259, ed. Doornbos, D.J., Academic Press.

Kennett, B.L.N. & Gudmundsson, O., 1996. Ellipticity corrections for seismic phases, *Geophys. J. Int.*, **127**, 40–48.

Kito, T. & Kruger, F., 2001. Heterogeneities in D″ beneath the southwestern Pacific inferred from scattered and reflected P-waves, *Geophys. Res. Lett.,* **28,** 2545–2548.

Kito, T., Krüger, F. & Negishi, H., 2004. Seismic heterogeneous struture in the lowermost mantle beneath the southwestern Pacific, *J. geophys. Res.,* **109,** B09304, doi:10.1029/2003JB002677.

Knittle, E. & Jeanloz, R., 1989. Simulating the core-mantle boundary: an experimental study of high-pressure reactions between silicates and liquid iron, *Geophys. Res. Lett.,* **16,** 609–612.

Labrosse, S., Hernlund, J. & Coltice, N., 2007. A crystallizing dense magma ocean at the base of the Earth's mantle, *Nature,* **450,** 866–869.

Mao, W.L. *et al.,* 2005. Iron-rich silicates in the Earth's D″ layer, *Proc. Natl. Acad. Sci.,* **102,** 9751–9753.

McNamara, A.K. & Zhong, S., 2005. Thermochemical structures beneath Africa and the Pacific Ocean, *Nature,* **437,** 1136–1139.

McNamara, A.K., Garnero, E.J. & Rost, S., 2010. Tracking deep mantle reservoirs with ultra-low velocity zones, *Earth planet. Sci. Lett.,* **299,** 1–9.

Montelli, R., Nolet, G., Dahlen, F.A., Masters, G., Engdahl, E.R. & Hung, S.H., 2004. Finite-frequency tomography reveals a variety of plumes in the mantle, *Science,* **303,** 338–343.

Mori, J. & Helmberger, D., 1995. Localized boundary layer below the mid-Pacific velocity anomaly identified from a PcP precursor, *J. geophys. Res.,* **100,** 20 359–20 365.

Müller, G., 1985. The reflectivity method—a tutorial, *J. Geophys.,* **58,** 153–174.

Nomura, R., Ozawa, H., Tateno, S., Hirose, K., Hernlund, J., Muto, S., Ishii, H. & Hiraoka, N., 2011. Spin crossover and iron-rich silicate melt in the Earth's deep mantle, *Nature,* **473,** 199–202.

Obayashi, M. *et al.,* 2011. P-wave tomogaphy of Northeastern China observed with NECESSArray, in *Proceedings of the AGU Fall Meeting,* San Francisco.

Obayashi, M., Yoshimitsu, J., Nolet, G., Fukao, Y., Shiobara, H., Sugioka, H., Miyamachi, H. & Gao, Y., 2013. Finite frequency whole mantle P-wave tomography: improvement of subducted slab images, *Geophys. Res. Lett.,* **40,** 5652–5657.

Oganov, A.R., Brodholt, J. & Price, G.D., 2001. The elastic constants of MgSiO₃ perovskite at pressures and temperatures of the Earth's mantle, *Nature,* **411,** 934–937.

Persh, S.E., Vidale, J.E. & Earle, P.S., 2001. Absence of short-period ULVZ precursors to PcP and ScP from two regions of the CMB, *Geophys. Res. Lett.,* **28,** 387–390.

Ranasinghe, N.R. *et al.,* 2015. Lg attenuation in Northeast China using NESECSSArray data, *Geophys. J. Int.,* **200,** 67–76.

Rawlinson, N. & Kennett, B.L.N., 2004. Rapid estimation of relative and absolute delay times across a network by adaptive stacking, *Geophys. J. Int.,* **157,** 332–340.

Revenaugh, J. & Meyer, R., 1997. Seismic evidence of partial melt within a possibly ubiquitous low-velocity layer at the base of the mantle, *Science,* **227,** 670–673.

Ritsema, J., Deuss, A., van Heijst, H.J. & Woodhouse, J.H., 2011. S40RTS: a degree-40 shear-velocity model for the mantle from new Rayleigh wave dispersion, teleseismic traveltime and normal-mode splitting function measurements, *Geophys. J. Int.,* **184,** 1223–1236.

Rost, S., Garnero, E.J., Williams, Q. & Manga, M., 2005. Seismological constraints on a possible plume root at the core-mantle boundary, *Nature,* **435,** 666–669.

Rost, S., Garnero, E. & Stefan, W., 2010a. Thin and intermittent ultralow-velocity zones, *J. geophys. Res.,* **115,** B06312, doi:10.1029/2009jb006981.

Rost, S., Garnero, E., Thorne, M.S. & Hutko, A.R., 2010b. On the absence of an ultralow-velocity zone in the North Pacific, *J. geophys. Res.,* **115,** B04312, doi:10.1029/2009jb006420.

Russell, S.A., Reasoner, C., Lay, T. & Revenaugh, J., 2001. Coexisting shear- and compressional-wave seismic velocity discontinuities beneath the central Pacific, *Geophys. Res. Lett.,* **28,** 2281–2284.

Schimmel, M. & Paulssen, H., 1997. Noise reduction and detection of weak, coherent signals through phase-weighted stacks, *Geophys. J. Int.,* **130,** 497–505.

Shibutani, T., Tanaka, A., Kato, M. & Hirahara, K., 1993. A study of P-wave velocity discontinuity in D″ layer with J-Array records: preliminary results, *J. Geomag. Geoelectr.,* **45,** 1275–1285.

Simmons, N.A., Forte, A.M. & Grand, S.P., 2006. Constraining mantle flow with seismic and geodynamic data: a joint approach, *Earth planet. Sci. Lett.,* **246,** 109–124.

Soldati, G., Boschi, L. & Forte, A.M., 2012. Tomography of core-mantle boundary and lowermost mantle coupled by geodynamics, *Geophys. J. Int.,* **189,** 730–746.

Stacey, F.D. & Davis, P.M., 2004. High pressure equations of state with applications to the lower mantle and core, *Phys. Earth planet. Inter.,* **142,** 137–184.

Steinberger, B. & Calderwood, A.R., 2006. Models of large-scale viscous flow in the Earth's mantle with constraints from mineral physics and surface observations, *Geophys. J. Int.,* **167,** 1461–1481.

Steinberger, B. & Holme, R., 2008. Mantle flow models with core-mantle boundary constraints and chemical heterogeneities in the lowermost mantle, *J. geophys. Res.,* **113,** B05403, doi:10.1029/2007JB005080.

Sun, D., Tan, E., Helmberger, D. & Gurnis, M., 2007. Seismological support for the metastable superplume model, sharp features, and phase changes within the lower mantle, *Proc. Natl. Acad. Sci.,* **104,** 9151–9155.

Sun, D., Helmberger, D.V., Jackson, J.M., Clayton, R.W. & Bower, D.J., 2013. Rolling hills on the core–mantle boundary, *Earth planet. Sci. Lett.,* **361,** 333–342.

Takeuchi, N. *et al.,* 2014. Upper mantle tomography in the Northwestern Pacific region using triplicated P waves, *J. geophys. Res.: Solid Earth,* **119**(10), 7667–7685.

Takeuchi, N., Morita, Y., Xuyen, N.D. & Zung, N.Q., 2008. Extent of the low-velocity region in the lowermost mantle beneath the western Pacific detected by the Vietnamese Broadband Seismograph Array, *Geophys. Res. Lett.,* **35**(5), L05307, doi:10.1029/2008GL033197.

Tan, E., Leng, W., Zhong, S.J. & Gurnis, M., 2011. On the location of plumes and lateral movement of thermochemical structures with high bulk modulus in the 3-D compressible mantle, *Geochem. Geophys. Geosyst.,* **12**(7), doi:10.1029/2011GC003665.

Tang, Y. *et al.,* 2014. Seismic evidence for a subduction-induced plume for the origin of Changbaishan volcanism in northeast China, *Nat. Geosci.,* **7,** 470–475.

Tao, K. *et al.,* 2014. Crustal structure beneath NE China imaged by NECESSArray receiver function data, *Earth planet. Sci. Lett.,* **398,** 48–57.

Thorne, M.S., Garnero, E.J., Jahnke, G., Igel, H. & McNamara, A.K., 2013. Mega ultralow velocity zone and mantle flow, *Earth planet. Sci. Lett.,* **364,** 59–67.

Trampert, J., Vacher, P. & Vlaar, N., 2001. Sensitivities of seismic velocities to temperature, pressure and composition in the lower mantle, *Phys. Earth planet. Inter.,* **124,** 255–267.

Trampert, J., Deschamps, F., Resovsky, J. & Yuen, D., 2004. Probabilistic tomography maps chemical heterogeneities throughout the lower mantle, *Science,* **306,** 853–856.

Tsuchiya, T., 2011. Elasticity of subducted basaltic crust at the lower mantle pressures: insights on the nature of deep mantle heterogeneity, *Phys. Earth planet. Inter.,* **188,** 142–149.

van der Hilst, R.D., Widiyantoro, S. & Engdahl, E.R., 1997. Evidence of deep mantle circulation from global tomography, *Nature,* **386,** 578–584.

Vidale, J.E. & Benz, H.M., 1992. A sharp and flat section of the core-mantle boundary, *Nature,* **359,** 627–629.

Weber, M. & Körnig, M., 1992. A search for anomalies in the lowermost mantle using seismic bulletins, *Phys. Earth planet. Inter.,* **73,** 1–28.

Wen, L. & Anderson, D.L., 1995. The fate of slabs inferred from seismic tomography and 130 million years of subduction, *Earth planet. Sci. Lett.,* **133,** 185–198.

Wicks, J.K., Jackson, J.M. & Sturhahn, W., 2010. Very low sound velocities in iron-rich (Mg, Fe)O: implications for the core-mantle boundary region, *Geophys. Res. Lett.,* **37,** L15304, doi:10.1029/2010GL043689.

Williams, Q. & Garnero, E.J., 1996. Seismic evidence for partial melt at the base of Earth's mantle, *Science,* **273,** 1528–1530.

Wysession, M.E., Okal, E.A. & Bina, C.R., 1992. Ths structure of the core-mantle boundary from diffracted waves, *J. geophys. Res.,* **97,** 8749–8764.

Wysession, M.E., Lay, T., Revenaugh, J., Williams, Q., Garnero, E.J., Jeanloz, R. & Kellogg, L.H., 1998. The D″ discontinuity and its implications, in *The Core-Mantle Boundary Region,* pp. 273–297, eds Gurnis, M., Wysession, M.E., Knittle, E. & Buffett, B.A., AGU.

Xu, Y. & Koper, K.D., 2009. Detection of ULVZ at the base of the mantle beneath the northwest Pacific, *Geophys. Res. Lett.,* **36,** L17301, doi:10.1029/2009GL039387.

Yamada, A. & Nakanishi, I., 1996. Detection of P-wave reflector in D″ beneath the south-western Pacific using double-array stacking, *Geopohys. Res. Lett.,* **23,** 1553–1556.

Yamada, A. & Nakanishi, I., 1998. Short-wavelength lateral variation of a D″ P-wave reflector beneath the southwestern Pacific, *Geophys. Res. Lett.,* **25,** 4545–4548.

Yao, J. & Wen, L., 2014. Seismic structure and ultra-low velocity zones at the base of the Earth's mantle beneath Southeast Asia, *Phys. Earth planet. Inter.,* **233,** 103–111.

Yoshida, M., 2008. Core-mantle boundary topography estimated from numerical simulations of instantaneous mantle flow, *Geochem. Geophys. Geosys.,* **9,** Q07002, doi:10.1029/2008GC002008.

Yoshida, M., 2012. Plume's buoyancy and heat fluxes from the deep mantle estimated by an instantaneous mantle flow simulation based on the S40RTS global seismic tomography model, *Phys. Earth planet. Inter.,* **210–211,** 63–74.

Young, M.K., Tkalčić, H., Bodin, T. & Sambridge, M., 2013. Global P wave tomography of Earth's lowermost mantle from partition modeling, *J. geophys. Res.,* **118,** 5467–5486.

Zhao, D., 2004. Global tomographic images of mantle plumes and subducting slabs: insight into deep Earth dynamics, *Phys. Earth planet. Inter.,* **146,** 3–34.